REPORTS@SCM

AN ELECTRONIC JOURNAL OF THE
SOCIETAT CATALANA DE MATEMÀTIQUES

On the relationship between singularity exponents and finite time Lyapunov exponents in remote sensed images of the ocean

*Lluïsa Puig Moner
Universitat Autònoma de Barcelona
lluisapuigmoner@gmail.com

*Corresponding author

Resum *(CAT)*

Els processos de transport i mescla horitzontals són clau per descriure la majoria de fenòmens a l'oceà. Les estructures lagrangianes coherents es defineixen com màxims locals dels exponents de Lyapunov finits i expliquen aquests processos. Cal però, una seqüència del camp de velocitats per estimar-los numèricament. Aquí, estudiem fins a quin punt aquests exponents es poden estimar mitjançant l'anàlisi singular de diferents imatges satèl·lit de l'oceà. L'anàlisi singular es basa en la descomposició d'un senyal en components fractals caracteritzats pels anomenats exponents de singularitat.

Abstract *(ENG)*

Horizontal transport and mixing are key to properly understanding changes in the global ocean. Lagrangian Coherent Structures explain those processes and are defined as the local maxima of Finite Size Lyapunov Exponents which can only be estimated by a long enough sequence of the velocity field. We discuss to which extend the exponents can be estimated by using only singularity analysis of remote sensed images of the ocean. Singularity analysis is based on the decomposition of a signal in fractal components characterised by the Singularity Exponents which we compare to the Lyapunov Exponents.

Keywords: *finite size Lyapunov exponents, singularity exponents, remote sensing, Lagrangian analysis, Eulerian analysis.*
MSC (2020): *76F20, 76-05, 76U60, 86A05.*

Received: *July 7, 2023.*
Accepted: *September 23, 2023.*

Societat Catalana de Matemàtiques

Institut d'Estudis Catalans

1. Introduction

Generally speaking, the ocean flows can either be described as laminar or turbulent. Motion in laminar circulation can be well characterized since neighbour particles advected by these flows track similar paths. In the turbulent case, movements are dominated by twirls, eddies and certain randomness. Particles that are close to each other might be widely separated later. Ocean circulation is described by the latter case.

Finite size Lyapunov exponents (FSLE) characterize the rate of separation of close trajectories and therefore, provide information of the dispersion processes and the Lagrangian coherent structures. The information provided by FSLE is enough to assess a major part of the circulation on the global ocean. The main disadvantage of using FLSE to asses dynamic information is that their estimation requires a long sequence of velocity field data. The main objective of this work is to understand the extent to which we can estimate FSLE by using only remote sensed images (without requiring the velocity field). For this, we will explore the functional relationship between the singularity exponents (SE) of the sea surface temperature (SST) signal and the FSLE. The former exponents represent the Eulerian description of dynamics while the latter represent the Lagrangian approach. In general, an autonomous system, with constant velocity fields presents an evident correspondence between Eulerian and Lagrangian descriptions. The same is not evident for turbulent systems.

The article is structured as follows. The first section includes the theoretical background of the Eulerian and the Lagrangian approaches. We provide the mathematical definition of the singularity and Lyapunov exponents, a discussion on how these exponents can describe the underlying dynamics and the introduction of a discrete and finite method to estimate them. The remaining sections are devoted to assess a preliminary functional relation to explain FSLE in terms of SST singularity exponents (SST SE). We compute the SE of sea surface temperature (SST) and absolute dynamic topography (ADT) following an algorithm based on the most unpredictable measure. FSLE are acquired from an external source. Finally, we asses a functional relationship between the exponents. We also evaluate the correspondence between SST SE and ADT SE which are theoretically equivalent.

2. Theoretical background

The rapid rotation of the Earth and the strong stratification of the essentially incompressible[1] water in the ocean generate turbulent dynamics in the open ocean. Indeed, the turbulence is not bidimensional but 3-D in the ocean. Satellite measurements can only capture the 2-D turbulence, but the ocean is 3-D turbulent. We could define two dimensional stream functions that approximate the motion in the ocean, although not always with the required accuracy. In fact, the dynamics in the ocean are characterized by having structures and areas where infinitesimal perturbations grow exponentially in time and thus it defines a chaotic system. Sections 2.1 and 2.2 respectively present the mathematical Lagrangian and Eulerian characterizations of the geometrical structures that describe the stream functions.

[1] $\nabla \mathbf{u} = 0$ for any compressible flow, where $\mathbf{u}$ is the velocity vector.

2.1 Characterization of Lagrangian coherent structures via finite Lyapunov exponents

Lagrangian finite time coherent structures (LCS)

On the definition of LCS: Consider the two-dimensional velocity field known for finite times

$$\dot{\mathbf{x}} = \mathbf{u}(\mathbf{x}, t)$$

with $\mathbf{x} \in \mathbb{R}^2$, $t \in \mathbb{R}$, and $\mathbf{u}$ as a continuously differentiable function on $\mathbf{x}$ and t. The trajectory defined by this field starting at time t_0 in $\mathbf{x_0}$ will be referenced as $\mathbf{x}(t, t_0, \mathbf{x_0})$. The map $\mathbf{F}_{\mathbf{t_0}}^{\mathbf{t}} : \mathbf{x_0} \to \mathbf{x}(t_0 + t, t_0, \mathbf{x_0})$ relates initial positions at t_0 to later positions at time $t_0 + t$ in the phase space.

Dynamics generated by the velocity field can be explained in terms of material lines. Particles moved by the flow advection with time form curves that are called material lines. We will denote them by $\mathcal{L}(t)$.

Definition 2.1 (Material line)**.** One parameter family of class C^1 curves satisfying $\mathbf{F}_{\mathbf{t_0}}^{\mathbf{t}}(\mathcal{L}(t_0)) = \mathcal{L}(t)$.

Given a material line $\mathcal{L}(t) \in \mathbb{R}^2$, $(\mathcal{L}(t), t)$ is a two dimensional invariant manifold in the extended phase space $\mathbb{R}^2 \times \mathbb{R}$.

Attracting and repelling material lines must be distinguished in terms of local stabilities and instabilities. They are defined over an open time interval $\mathcal{I}$ within $\mathbb{R}$.

- **Attractive $\mathcal{L}$(t) over $\mathcal{I}$:** A material line such that any particle close to it exponentially converges to that manifold at some time in $\mathbb{R}$.

  Given a material line $\mathcal{L}(t)$ and a concrete trajectory $\mathbf{x}(t) \in (\mathcal{L}(t), t)$ consider $T_{\mathbf{x}}\mathcal{L}(t)$ as the two-dimensional tangent plane of $(x(t), t)$ in the extended phase space.

  $\mathcal{L}(t)$ is an attractive material line if there exists a constant $\nu > 0 \in \mathbb{R}$ and a smooth family of one-dimensional subspaces $E^s(t)$ in the extended phase space tangent to $T_{\mathbf{x}}\mathcal{L}(t)$ such that

  $$\nabla \mathbf{F}_{t_0}^{t}(\mathbf{x}(t_0))E^s(t_0) = E^s(t) \quad \text{and} \quad \|\nabla \mathbf{F}_{\mathbf{t_0}}^{\mathbf{t}}(\mathbf{x}(t_0))|_{E^s(t_0)}\| \leq e^{-\nu(t-t_0)}$$

  for $t_0, t \in \mathcal{I}$.

- **Repelling $\mathcal{L}$(t) over $\mathcal{I}$:** An attractive material line over $\mathcal{I}$ backwards in time. This means that any perturbation of the position of a particle initially on $\mathcal{L}(t)$ will exponentially diverge from $\mathcal{L}(t)$.

We call *finite time hyperbolic line* over $\mathcal{I}$ any material line that is attractive or repulsive.

The stability of the material lines changes over time. *Lagrangian coherent structure boundaries* are defined as material lines with locally the longest or shortest stability or instability times. Therefore, we can understand them as linearly stable or unstable material lines. In other words, *Lagrangian coherent structures* (LCS) retain the stability of the hyperbolic lines over time.

Given a material line L, we introduce the following scalar fields $T_{\mathbf{L}}(\mathbf{x_0}, t_0, t)$ to rigorously define LCS. For any initial condition $\mathbf{x_0}$ at time $t_0 \in [t_{-1}, t_1]$ we consider $T_{\mathbf{L1}}(\mathbf{x_0}, t_0, t_1) = \frac{1}{t_1 - t_0} \int_{\mathcal{I}_{\mathbf{L1}}} dt$, where $\mathcal{I}_{\mathbf{L1}}$ is the maximal open set within $[t_0, t_1]$ over which the trajectory $\mathbf{x}(t, t_0, \mathbf{x_0})$ remains in a material line of stability type **L1**.

Definition 2.2 (Lagrangian coherent structure)**.** Local extrem of the scalar fields $T_{\mathbf{L1,2}}(\mathbf{x_0}, t_0, t)$.

This definition yields to four distinct types of LCS. Let $\mathcal{C}(t)$ be a Lagrangian coherent structure boundary over time.

- $\mathcal{C}(t)$ as local maximizer of $\mathbf{T_L}$: Structure capturing or pushing away particles for locally the longest times on both sides of $\mathcal{L}(t)$.
- $\mathcal{C}(t)$ as local minimizer of $\mathbf{T_L}$: This case explains LCS's behaviour near a wall (physical barrier). Concretely their approach to the wall forward in time.

At larger distances from any wall, the coherent structures boundaries are local maximizers of $T_{\mathbf{L1}}$ and $T_{\mathbf{L2}}$ fields. In the framework of the ocean dynamics, potential walls are physical boundaries such as a coast or ice edge which are not considered in this project and therefore, LCS as local minimizers of time fields are no longer considered in our discussion.

On the detection of LCS: According to the previous definition, if we consider the maximal net growth of a unit vector transverse to a LCS, it has to be locally the largest over $\mathcal{I}$. This holds for either attractive or repelling structures.

Consider a repelling structure $\mathcal{C}(t)$ and $\mathbf{x_0}$ a point in $\mathcal{C}(t_0)$. $\nabla_{\mathbf{x_0}}\mathbf{F}^{\mathbf{t}}_{\mathbf{t_0}}$ is the linearized flow map around $\mathbf{x_0}$ so the following equation describes the propagation of a unit vector $\mathbf{e}_{\mathbf{t_0}}$ selected at $\mathbf{x_0}$ not tangent to $\mathcal{C}(t_0)$ along the trajectory $\mathbf{x}(t, t_0, \mathbf{x_0})$. ($\mathbf{e}_{\mathbf{t_0}}$ is identified with $\mathbf{v}$.)

$$\mathbf{e}_t(\mathbf{x_0}) = (\nabla_{\mathbf{x_0}}\mathbf{F}^{\mathbf{t}}_{\mathbf{t_0}})\mathbf{e}_{\mathbf{t_0}}.$$

We concluded that repelling coherent structures are the maximizers of $|\mathbf{e}_{\mathbf{t_0}}(\mathbf{x_0})|$ over all possible $\mathbf{e}_{\mathbf{t_0}}$ and $\mathbf{x_0}$. We define $\mathcal{E}^t_{t_0}(\mathbf{x_0})$ as the maxim resulting propagation over all choices of $\mathbf{e}_{\mathbf{t_0}}$.

$$\mathcal{E}^t_{t_0}(\mathbf{x_0}) = \max_{|\mathbf{e}|=1} |(\nabla_{\mathbf{x_0}}\mathbf{F}^{\mathbf{t}}_{\mathbf{t_0}})\mathbf{e}_{\mathbf{t_0}}| \equiv \|(\nabla_{\mathbf{x_0}}\mathbf{F}^{\mathbf{t}}_{\mathbf{t_0}})\|,$$

where $\|\ \|$ is the operator norm $\|\mathbf{A}\| = \max_{|\mathbf{x}|=1} |\mathbf{A}\mathbf{x}|$ for a general matrix $\mathbf{A} \in \mathbb{R}^2$. By definition, $\|\mathbf{A}\|$ is the square root of the maximal eigenvalue of the positive matrix $\mathbf{A}^T\mathbf{A}$ namely $\|\mathbf{A}\| = \lambda_{\max}(\mathbf{A}^T\mathbf{A})$, so $\mathcal{E}^t_{t_0}(\mathbf{x_0})$ can be rewritten as

$$\begin{aligned}
\mathcal{E}^t_{t_0}(\mathbf{x_0}) &= \sqrt{\lambda_{\max}((\nabla_{\mathbf{x_0}}\mathbf{F}^{\mathbf{t}}_{\mathbf{t_0}})^T(\nabla_{\mathbf{x_0}}\mathbf{F}^{\mathbf{t}}_{\mathbf{t_0}}))},\\
\dot{\mathbf{x}}(t) &= \Lambda\mathbf{x}(t),\\
\mathbf{x}(t) &= \mathbf{x}(t_0)e^{\Lambda(t-t_0)} = \mathbf{x}(t_0)\mathcal{E}^t_{t_0}(\mathbf{x_0}).
\end{aligned}$$

This is a measure of the maximal growth over the most repelling direction in $\mathbf{x_0}$. $\mathbf{x_0}$'s with large values of $\mathcal{E}^t_{t_0}(\mathbf{x_0})$ define the LCS.

Finite size and time Lyapunov exponents approach to LCS

We define the finite time Lyapunov exponent (FTLE) at $(t, t_0, \mathbf{x_0})$ as $\Lambda(t, t_0, \mathbf{x_0})$ following the next equation

$$\Lambda(t, t_0, \mathbf{x_0}) = \frac{1}{2(t-t_0)} \log_e\Big(\lambda_{\max}((\nabla_{\mathbf{x_0}}\mathbf{F}^{\mathbf{t}}_{\mathbf{t_0}})^T(\nabla_{\mathbf{x_0}}\mathbf{F}^{\mathbf{t}}_{\mathbf{t_0}}))\Big).$$

Following the formality in the previous section, the local maxima of $\mathcal{E}^t_{t_0}(\mathbf{x_0})$ coincides with the local maxima of the finite time Lyapunov exponent since they are related as

$$\mathcal{E}^t_{t_0}(\mathbf{x_0}) = e^{\Lambda(t,t_0,\mathbf{x_0})(t-t_0)}.$$

Therefore, $\mathbf{x_0'}s$ locally maximizing of FTLE is a good approach to LCS. As the relative stretching tends to grow rapidly, it is more convenient to work with FTLE that are not attenuated by the factor $(t - t_0)$ than to directly work with $\mathcal{E}^t_{t_0}(\mathbf{x_0})$.

Finally, we introduce the concept of finite size Lyapunov exponents (FSLE) as an equivalent to FTLE. Accordingly to [7] they are defined as

$$\Pi(r, t_0, \mathbf{x_0}) = \frac{\log_e(r)}{2(t - t_0)}, \tag{1}$$

where $t - t_0$ is the minimum time for which $r = \lambda_{\max}((\nabla_{\mathbf{x_0}}\mathbf{F}^{\mathbf{t}}_{\mathbf{t_0}})^T(\nabla_{\mathbf{x_0}}\mathbf{F}^{\mathbf{t}}_{\mathbf{t_0}}))$.

It is key to understand the intuitive idea of finite Lyapunov exponents as a measure of the exponential growth of small perturbations. In this sense, a more intuitive definition equivalent to (1) is associating the FSLE to the maximum value of

$$\boldsymbol{\lambda}(\mathbf{x_0}, t_0, \boldsymbol{\delta_0}, \delta_f) = \frac{1}{\tau}\log\left(\frac{\delta_f}{|\boldsymbol{\delta_0}|}\right)\frac{\boldsymbol{\delta_0}}{|\boldsymbol{\delta_0}|}$$

over all the accessible directions of $\boldsymbol{\delta_0}$.

τ is the backward time that the two trajectories take starting at time t_0 at $\mathbf{x_0}$ and $\mathbf{x_0}+\boldsymbol{\delta_0}$ to respectively reach the prescribed separation $\delta_f > |\boldsymbol{\delta_0}|$.

FTLE and FSLE have units of time^{-1}. Both exponents represent a finite time, respective size, description. Therefore only under certain conditions do FSLE ridges imply close FTLE ridges which in turn indicate the existence of an hyperbolic LCS [4]. In this work we assume their total equivalence as detectors of LCS so FSLE highlight the transport barriers that control the horizontal exchange of water in and out of eddy cores.

For ocean signals, we only dispose of finite and discrete time sequences of images of discrete spatial resolution, namely Δx. This determines the implementation of algorithms to compute FTLE and FSLE. According to the previous definitions, FTLE are defined over a prescribed time while FSLE are defined over a prescribed final separation. Concretely, FSLE depend on the relative size of $\boldsymbol{\delta_0}$ and δ_f against Δx. Choosing $\boldsymbol{\delta_0} \ll \Delta x$ would imply that no point lying further than δ_0 of any grid point would ever be tested. Therefore, in the regions where the signal is stretching, the method would give a discontinuous sampling of the structures. Instead, if $\boldsymbol{\delta_0} \gg \Delta x$, the algorithm would lead to a loss of spatial resolution since the same smeared stretching manifold would be detected on several grid points. The previous simple argument shows the convenience of using a value of $\boldsymbol{\delta_0}$ close to Δx. The second length scale δ_f determines the size of the structures willing to be evaluated. This is the reason why we choose FSLE and not FTLE. We prioritize controlling the length of the structures we want to detect above their duration.

2.2 Singularity analysis for remote sensed images of the ocean

Singularity analysis is the process of obtaining a dimensionless measure of the degree of irregularity at each point of a given signal $s(\mathbf{x})$. This measure is known as the singularity exponent and it refers to the analysis of singularities[2] of differentiable functions.

[2]Singularities as points, where the mathematical object ceases to be well-behaved by lacking differentiability or analytically.

Singularity exponents

Different implementations of computation for singularity exponents are possible. Here we expand on the most usual meaning in the theory of complex systems. This is understanding SE as the continuous extension of continuity or differentiability. SE are dimensionless and track transitions independently of their amplitude. Therefore, even subtle structures can be detected on their images.

Consider the pseudo-Taylor expansion ([9, 11]) of the signal

$$s(\mathbf{x}+\mathbf{r}) - s(\mathbf{x}) = \alpha(\mathbf{x}) r^{H(\mathbf{x})} + \mathcal{O}(r^{H(\mathbf{x})}), \quad r \to 0.$$

If any point $\mathbf{x}$ in the signal behaves according to the previous expansion for a concrete value of $\alpha(\mathbf{x})$, the non necessarily integer exponent $H(\vec{x})$ is defined as the singularity exponent. It is also known as the Hölder exponent measuring the degree of regularity (positive value) or irregularity (negative value) of the signal. Negative exponents characterize regularity. Exponents vanishing to zero imply continuity but non-differentiability. Values in the range $(0, 1)$ are found in points where the signal is more regular than a continuous one but still not differentiable. Finally, 1, 2, and further k integers imply k-differentiability.

Any continuous function $\psi(\mathbf{x})$ can be recognised as a wavelet or mother wavelet. For efficiency reasons, common wavelets are characterized by properties such as differentiability, orthogonality, compact support, symmetry, and vanishing moment [5].

Definition 2.3. The *wavelet projection* or *continuously wavelet transform* of a signal $f(\mathbf{x})$ on the mother wavelet ψ in $\mathbf{x}$ and with a scale scope r is

$$\begin{aligned} \mathcal{T}_\psi s(\mathbf{x}, r) &= \int ds(\mathbf{y}) \frac{1}{r^d} \psi\left(\frac{\mathbf{x}-\mathbf{y}}{r}\right), \\ \mathcal{T}_\psi s(\mathbf{x}, r) &= \alpha_\psi(\mathbf{x}) r^{H(\mathbf{x})} + \mathcal{O}(r^{H(\mathbf{x})}), \quad r \to 0, \\ \mathcal{T}_\psi \nabla s(\mathbf{x}, r) &= \alpha_\psi(\mathbf{x}) r^{h(\mathbf{x})} + \mathcal{O}(r^{h(\mathbf{x})}), \quad r \to 0, \end{aligned} \tag{2}$$

where d is the dimension of the signal domain.[3] For $\psi(\mathbf{x})$ to be a wavelet for the continuous wavelet transform, there is an admissibility criterion implying that the first order moment must vanish to zero.

The wavelet projection is the convolution of the signal with a re-sized version of the mother wavelet $\psi(\mathbf{x})$. The resolution parameter r regulates the range of the wavelet. For its construction, it conveys redundant information but is well adapted to detect transitions in data.

It is proved that for signals obeying (2), their wavelet projections also scale with the same power law over r (see [3]). This power law is well adapted to filter long range correlations and just detects local structure that represent the continuous scale of changes.

In practice, the computation of the exponents from real discrete data has a rough resolution even using wavelet transformations. Wavelet projections of the modulus of the gradient lead to a more precise determination of SE with improved spatial resolution. For any signal scaling as a power law in r, its gradient scales similar. Understanding the singularity exponents as a continuous measure of differentiability, the gradient operator lessens by one unit the differentiability degree. This implies that the SE of the gradient, let it be $h(\mathbf{x})$, is related to the SE of the proper signal $H(\mathbf{x})$ like

$$h(\mathbf{x}) = H(\mathbf{x}) - 1.$$

[3] In the two dimensional case we work, $d = 2$.

In this project we will consider SE associated to gradient measures. Therefore, the nomenclature for SE will be $h(\mathbf{x})$. There exists a theoretical bound for $h(\mathbf{x})$ in range $(-1, 2)$.[4]

Multifractal signal and the most singular component (MSC)

One way to show that a given image possess multifractal structure is to construct a positive measure μ which assigns positive value to any set $\mathcal{A}$. The measure must take into account any sharp transitions in $\mathcal{A}$. We define the measure in terms of its density like

$$\mu(\mathcal{A}) = \int_{\mathcal{A}} d\mu(\mathbf{x}) \quad \text{with} \quad d\mu(\mathbf{x}) \equiv |\nabla s|(\mathbf{x})\, d\mathbf{x}.$$

The behaviour of any particular point $\mathbf{x}$ can be characterized in terms of the evolution of the measure of balls centered on $\mathbf{x}$ of radius r denoted as $\mathcal{B}_r(\mathbf{x})$.

The measure μ defines a *multifractal* if it is characterized by unique exponent $h(\mathbf{x})$ and coefficient $\alpha(\mathbf{x})$ such that

$$\mu(\mathcal{B}_r(\mathbf{x})) = \alpha(\mathbf{x}) r^{d+h(\mathbf{x})} + \mathcal{O}(r^{d+h(\mathbf{x})}). \tag{3}$$

$\mathcal{O}(r^{d+h(\mathbf{x})})$ is negligible in comparison with $r^{d+h(\mathbf{x})}$.

The exponent $h(\mathbf{x})$ in (3) attains the definition of singularity exponent for the gradient measure μ.

$\alpha(\mathbf{x})$ depends on the particular metrics in the definition of the ball and the scaling unit for r, but does not provide information about changes in scale. All the information about the evolution under changes in r is contained in the SE which is independent of metrics and scaling units.

As discussed in the previous section, applying a wavelet projection over the measure leads to the same power law that permits a more efficient estimation of the exponents. This is

$$\mathcal{T}_\psi \mu(\mathbf{x}, r) = \alpha_\psi(\mathbf{x}) r^{h(\mathbf{x})} + \mathcal{O}(r^{h(\mathbf{x})}) \quad \text{equivalent to} \quad m(\mathbf{x}, r) = \alpha(\mathbf{x}) r^{h(\mathbf{x})} + \mathcal{O}(r^{h(\mathbf{x})}) \tag{4}$$

for any $m(\mathbf{x}, r)$ defined measure of unpredictability.

Definition 2.4. A *fractal component* F_h is defined as the set of points of an image having the same exponent h.

$$F_h = \{\mathbf{x} \text{ such that } h(\mathbf{x}) = h\}.$$

The decomposition of a signal as the union of different fractal components is called a multifractal decomposition of the signal.

Fractal components are of a very irregular nature. The odd arrangement of the points in fractal sets can be characterized by counting the number of points contained inside a given ball of radius r. We define this number as $N_r(h, \Delta_h)$, where Δ_h is a threshold for admissibility in F_h. As $r \to 0$ the following power law holds ([10])

$$N_r(h, \Delta_h) \approx r^{D(h)}.$$

The exponent $D(h)$ quantifies the size of the set of pixels with singularity h as the image is covered with small balls of radius r. It is known as the *fractal dimension* of the associated fractal component F_h. The

[4] The lower bound comes from the physical limit that no point from a signal tracing of the ocean dynamics can infinitely diverge. The upper bound is consequence of the lower bound and the transitional invariance of the signal.

function $D(h)$ defined $\forall h \in (-1, 2)$ for signals of ocean tracers is called the dimension spectrum of the multifractal image. Fractal components usually range from dimension one, $D(h) \approx 1$, for the most singular values (curve-like components), to dimension $D(h) \approx 2$ for higher exponents that extend on less definite areas.

The multifractal behaviour allows a strong hierarchical organization in images. This organization is explained in terms of the most singular components (MSC).

Definition 2.5. The *most singular component* (MSC)[5] is the fractal component

$$F_\infty = \{\mathbf{x} \text{ such that } h(\mathbf{x}) \in]h_\infty - \Delta, h_\infty + \Delta[\},$$

where h_∞ is the minimal value over the domain and Δ a threshold.

There exists a unique operator associated to the most singular component (see [8]) that reconstructs the image. For that, the MSC is recognised as the more informative component.

Estimation of singularity exponents using the unpredictable point manifold

Signal reconstruction from a partial set of the gradient is the key concept to define a wavelet that precisely identifies SE. We discussed how one can properly reconstruct any signal from the gradient of MSC points. Therefore MSC can be identified as the less predictable set of points. The unpredictable point manifold (UPM) consists in the set of points that cannot be reconstructed from others so it can be associated to the MSC.

To numerically characterize the unpredictable point manifold, a measure of unpredictability for each point $\mathbf{x}$ has to be settled. It can be identified as $\mathcal{T}_\psi \mu$ in (4) and singularity exponents can be derived from it.

The following is a punctual estimation of the singularity exponent $h(\mathbf{x})$ defined in (4).

$$h(\mathbf{x}) = \frac{\log\left(\frac{\mathcal{T}_\psi \mu(\mathbf{x}, r_0)}{\langle \mathcal{T}_\psi \mu(\mathbf{x}, r_0) \rangle}\right)}{\log r_0} + \mathcal{O}\left(\frac{1}{\log r_0}\right), \quad h(\mathbf{x}) \approx \frac{\log\left(\frac{m(\mathbf{x})}{\langle m \rangle}\right)}{\log r_0},$$

where $m(x)$ is an effective UPM-measure for 2D images. For more information on the algorithm, please contact the author. The algorithm is part of an internal note of the Institute of Marine Sciences in Barcelona.

3. Lyapunov and singularity exponents in a global scale and empirical functional relation between them

The results presented here are obtained analysing the following data: (i) *Backward-in-time, finite size Lyapunov exponents and orientations of associated eigenvector*. The exponents are distributed on a 0.25^0 grid on a global coverage and have units of day^{-1}. Figure 2a contains a map of FSLE from this product.

[5] MSC might also be found as the most singular manifold (MSM) in the bibliography.

(ii) SST and ADT global, two-dimensional remote sensed signals from Copernicus Marine Service with spatial resolution of 0.25^0 and daily temporal resolution. The computation of the exponents is based on an estimation of the unpredictable measure (image processing) introduced in 2.2.

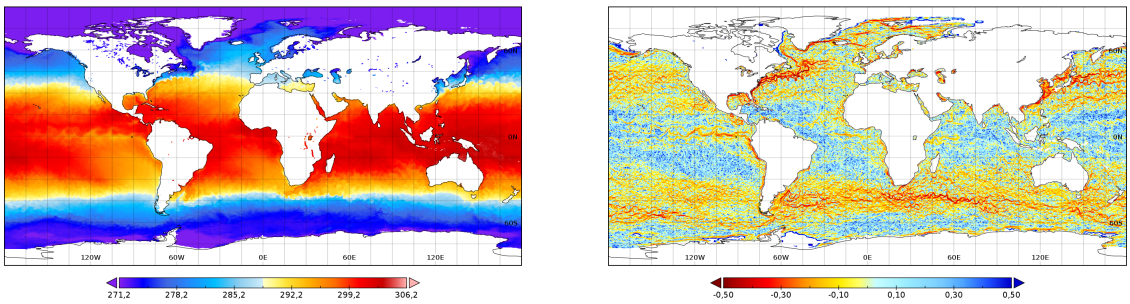

(a) (b)

Figura 1: (a) SST global image from [2] *Global Ocean OSTIA Sea Surface Temperature and Sea Ice Analysis Results* for January 25th, 2022. Temperatures in the color bar are expressed in Celsius degrees. (b) Global image of the singularity exponents (SE SST) computed from (a).

The SST SE map is qualitatively as expected. There are some areas of the ocean known to be the most energetic ones and having the most important streams. Some of these areas are the East coast of North America, with the Gulf Stream, and the Antarctic Circumpolar Current that connects the Southern Ocean. We see in our results that these areas have the most negative exponents with well defined fractal components. In the areas showing the most negative exponents, complex undulated shapes, wave-like instabilities, eddy-like patterns, and intense vortices are distinguished. Those areas are associated to the most singular component. Their organization in curve-like structures justifies their fractal dimension to be $D(h) \approx 1$. Areas with positive exponents are less defined and do not present a clear structure nor intense vortices. The organization in fractal components is more confusing so their fractal dimension is closer to $D(h) \approx 2$; the maximal possible.

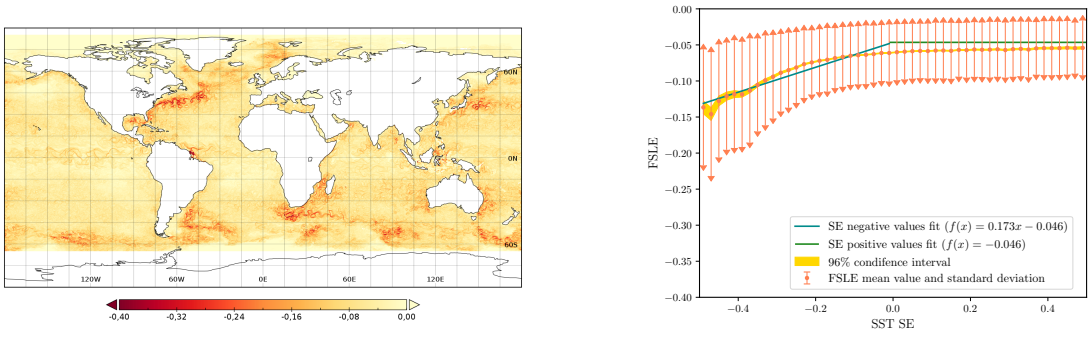

(a) (b)

Figura 2: (a) Backward-in-time, finite size Lyapunov exponents and orientations of associated eigenvectors product in [1] for January 25th, 2022. (b) Global fit and piecewise function explaining the relationship between FSLE and SST SE of the global maps 2a and 1b.

Analysing the FSLE, one can distinguish boundaries of coherent structures that coincide with the previously described as the most energetic areas. The boundaries are defined by curve-like patterns with the most negative values of the exponents (i.e. the regions with the strongest exponential attractive material lines). Visually, the structures detected by singular analysis and Lagrangian coherent structures seem to effectively have a correspondence, at least with their location on the maps. The analysis of data by density plots shows that most of the SE exponents are found in the range $[-0.1, 0.1]$ and the Lyapunov ones in the range $[-0.1, -0,05]$. In fact, the most negative values of FSLE are only associated to the most negative values of SST SE. Nevertheless, negative values of SE SST are present in the whole range of FSLE values.

To define an empirical functional relation between SST SE and FSLE we compute the density and normalized density plots. Then we take the average over FLSE values (see Figure 2b). This is considering the mean value of the FSLE values x_i associated to each SE (SE values ordinated in bins of 0.02 units width). Each point includes the standard deviation representation of the average value it represents $\sigma = \sqrt{\frac{\sum_{n=1}^{N}(x_i-\bar{x})^2}{N-1}}$ and the 96% interval of confidence. Then, the functional relation (FSLE in terms of SE) is assessed over this averaged plot, constructing a continuous piecewise function. For the negative domain of SE we have linearly fitted the values from the previous average. We have associated the constant value $f(SE = 0)$ to the positive SE. f represents the linear fit. This is only a preliminary estimation of the relation.

The coefficient of the regression between FSLE and negative SE SST is $r^2 = 0.88$. We observe that the relationship between these two variables is not completely linear. However, in this analysis we simplify and we keep on using this preliminary linear fit. This linear fit has some limitations: (i) the average is a measure of the most frequent value for a given SST SE value, but the standard deviation shows that there is a large variability that will not be taken into account in this approach. (ii) the mean value is affected by outliers and in this case produces an overestimation of the most negative FSLE values. Besides the limitations of the linear fit approach, the data itself also has some accuracy limitations and the methods applied for deriving FSLE and SE also add uncertainty to the full process.

Reconstruction of FSLE from SST SE

We have reconstructed the FSLE's map using the SST SE map and the functional relation established in Figure 2b. We observe several limitations of the applied approach: (i) By definition, the areas having the less singular exponents, namely positive, are associated to constant, close to zero values of FSLE. This is a first limitation of our reconstruction because the real FSLE map, although having areas with light variability does not have any constant part. (ii) The range of variation of the reconstructed FSLE $(-0.2 : 0)$ is lower than the one of the original FSLE values $(-0.4 : 0)$. This is in part because of the effect of the linear fitting that does not allow recovering the most negative values. In addition, the use of the average FSLE to define the functional relation leads to a limited accuracy given by the variability of the FSLE around this average. (iii) Since the functional relation we establish is linear, the negative SE in the reconstructed map has the same pattern as the original SE map 1b. Here we compare the FSLE original map 2a and the reconstructed one. The figure shows the percentage of points where the difference between reconstructed and actual FSLE values (y-axis) is lower than a threshold (x-axis) for the same map used in the linear fit (no independent assessment, orange line) and for a different map (independent assessment, blue line). Both lines remain quite close one to the other with a small degradation for the independent map. We see that with this approach the reconstructed FSLE describes the 70% of the map with an accuracy of 0.05.

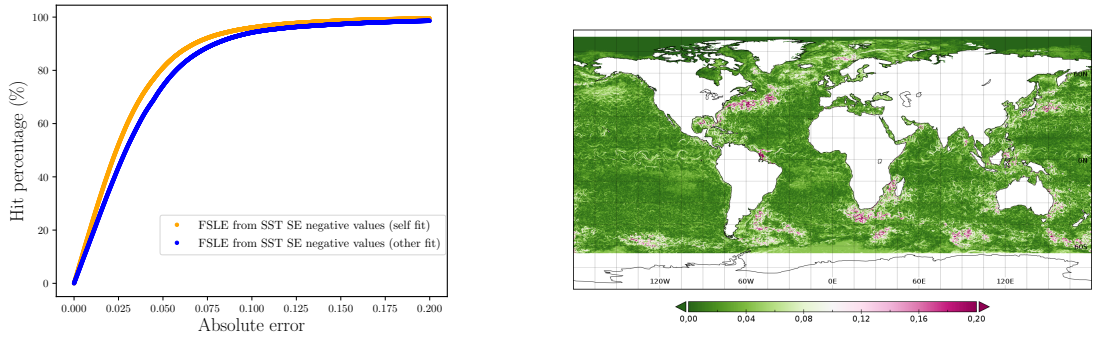

(a) (b)

Figura 3: (a) Hit percentage for the global reconstructed map for the same day the functional relation has been derived the 25th January 2022 (self fit), and SE SST map of another day (8th June, 2021). (b) Absolute error between the FSLE reconstructed map and the AVISO+ map 2a.

The map of the differences between reconstructed and actual FSLE values reveals that the reconstruction especially fails to predict the most negative exponents (for the limitations above described). See Figure 3b.

3.1 High energic regions

Finally, we assess up to which extent the global relation found in Figure 2b is also accurate at regional scales. We have analysed the following three areas: (i) Gulf Stream area in East Coast of North America: $[75W, 30W]$ $[30N, 60N]$. (ii) Angulas current area in South Africa: $[0E, 45E$ E$]$ $[60S, 30S]$. (iii) South Atlantic current area in South America: $[75W, 30W]$ $[60S, 30S]$.

The patterns of the functional relation are the same. The reduced number of pixels used in those regional plots make them more rough than the global ones. In future work we plan to use a larger time series of maps (for both global and regional assessment) in order to derive more robust density plots.

The linear fitting of the average FSLE value as function of the SST SE is also consistent with the one of the global maps. However we observe a constant offset between the regional and the global fitting. We associate these differences to the background high energy level of the selected regions.

Comparison between singularity exponents from ADT and SST

Finally, we have repeated the previous analysis but changing the SST SE for the ADT SE. From a theoretical point of view, both SE should be equal and both of them should be in correspondence with the streamlines. However, we observe that the accuracy of the different acquisitions is also a source of uncertainty affecting our results.

Qualitatively, comparing the maps representing the exponents they present the same large scale features. However, some important differences between both exponents appear. The most negative SST SE are organized in smoother and narrower curves with less negative SE values than the ADT SE. This is because of the effective spatial resolution of each product that is defined by the accuracy of the different instrument measuring the data and the different data processing algorithms.

4. Conclusions

The first objective of this paper is to understand two different mathematical concepts that describe the state of the ocean.

The second objective is to assess up to which extent the structures defined by the LCS and by the different multifractal components are related. The most negative FLSE are associated with the transport barriers. In our comparison we observe that positive SST SE are associated with the FLSE with values closest to zero, while the most negative SST SE present a monotonic growing relation with FSLE. We have linearly fitted negative SST SE with FSLE and we have assessed this relation. This approach allows representing 70% of the FSLE with an accuracy of 0.05. This analysis is the first step to understanding how these two exponents are related. During the study some limitations have been identified: The linear fitting overestimates the most negative FSLE. In the future we plan to fit with nonlinear functions to better estimate the most negative FSLE. We observe constant offset between the regional and the global fitting. We associate these differences to the background high energy level of the selected regions. This suggests that depending on the accuracy required in future applications, having regional fittings could be more appropriated than global ones.

We have selected the SST as the main ocean variable to be used to compute the reconstructed FSLE. This intrinsically assumes that the SE from any ocean variable are equal (this assumption is based on [6]). However, in practice, because of the different accuracy of the available data, we have also observed that there are significant differences between the SST SE and ADT SE. This leads to distinct functional relations between the FSLE and the SE. In order to address this in the future we plan to use an extended temporal series of satellite images. This would allow us to derive a more robust relationship between FSLE and SE. With this we will assess which are the strengths and limitations of using one ocean variable or the other. Besides, having larger temporal series will allow us to assess the temporal stability of the relationship between FSLE and SE. Finally, we have also provided an estimation of the uncertainty associated to the reconstructed FSLE which is based on the difference between actual and reconstructed values. There are other metrics that could provide valuable information for marine and maritime applications. For example the correspondence among the geometrical structures of both Lyapunov and singular exponents.

Acknowledgements

I want to thank my supervisors Estrella, Antonio, and Alvaro for guiding me through the project and sharing their knowledge. Without them, this study would not have been possible.

References

[1] CFOSAT science team, Aviso +, Online; accessed 2022-02-18. https://www.aviso.altimetry.fr/.

[2] Copernicus Marine Service, Copernicus, Online; accessed 2022-02-18. https://resources.marine.copernicus.eu/products.

[3] B. Jawerth, W. Sweldens, Wavelet transform maxima and multiscale edges, in: *An Over-*

view of the Theory and Applications of Wavelets, Y.-L. O, Ying-Lie, A. Toet, D. Foster, H.J.A.M. Heijmans, P. Meer, (eds), Springer Berlin Heidelberg, Berlin, Heidelberg, 1994, pp. 249–274.

[4] D. Karrasch, G. Haller, Do finite-size Lyapunov exponents detect coherent structures?, *Chaos* **23(4)** (2013), 043126, 11 pp.

[5] W.K. Ngui, M.S. Leong, L.M. Hee, A.M. Abdelrhman, Wavelet Analysis: Mother Wavelet Selection Methods, *Applied Mechanics and Materials* **393** (2013), 953–958.

[6] V. Nieves, C. Llebot, A. Turiel, J. Solé, E. García-Ladona, M. Estrada, D. Blasco, Common turbulent signature in sea surface temperature and chlorophyll maps, *Geophysical Research Letters* **34(23)** (2007), L23602.

[7] R. Peikert, A. Pobitzer, F. Sadlo, B. Schindler, A Comparison of Finite-Time and Finite-Size Lyapunov Exponents, in: *Topological Methods in Data Analysis and Visualization III. Theory, Algorithms, and Applications*, P.T. Bremer, I. Hotz, V. Pascucci, R. Peikert (eds), Math. Vis., Springer, Cham, 2014, pp. 187–200.

[8] A. Turiel, A. del Pozo, Reconstructing images from their most singular fractal manifold, *IEEE Trans. Image Process.* **11(4)** (2002), 345–350.

[9] A. Turiel, J. Isern-Fontanet, E. García-Ladona, J.A. Young, Detection of wave fronts in the Indian Ocean from geostationary sunglint satellite imagery, *International Journal of Remote Sensing* **28(17)** (2007), 3953–3962.

[10] A. Turiel, N. Parga, The Multifractal Structure of Contrast Changes in Natural Images: From Sharp Edges to Textures, *Neural Computation* **12(4)** (2000), 763–793.

[11] A. Turiel, J. Solé, V. Nieves, J. Ballabrera-Poy, E. García-Ladona, Tracking oceanic currents by singularity analysis of Microwave Sea Surface Temperature images, *Remote Sensing of Environment* **112(5)** (2008), 2246–2260.